

AN ABSTRACT OF THE THESIS OF

Louis Maizy for the degree of Master of Science in Physics presented on December 3, 2012.

Title: Terahertz Transmission & Spectroscopy of Vertically Grown Multi-Walled Carbon Nanotube Forests

Abstract approved: _____

Yun-Shik Lee

In this thesis, I present studies in the field of terahertz [THz] spectroscopy. It covers both the generation and detection of ultra-fast broadband THz pulses, as well as the transmission properties of vertically grown multi-walled carbon nanotube forests [MWCNTs]. We have found that these vertically grown MWCNTs respond strongly to THz radiation and exhibit an anisotropic optical response. The analysis done was a simplified model that is frequency-independent, which led to discrepancies between the theoretical and experimental data. This suggests that the response of the CNTs is frequency-dependent, and further, more complex analysis is required to fully describe their properties.

©Copyright by Louis Maizy

December 3, 2012

All Rights Reserved

Terahertz Transmission & Spectroscopy of Vertically Grown Multi-Walled Carbon Nanotube
Forests

by

Louis Maizy

A THESIS

submitted to

Oregon State University

in partial fulfillment of
the requirements for the
degree of

Master of Science

Presented December 3, 2012
Commencement June 2013

Master of Science thesis of Louis Maizy presented on December 3, 2012

APPROVED:

Major Professor, representing Physics

Chair of the Department of Physics

Dean of the Graduate School

I understand that my thesis will become part of the permanent collection of Oregon State University libraries. My signature below authorizes release of my thesis to any reader upon request.

Louis Maizy, Author

ACKNOWLEDGEMENTS

Academic

I would first like to thank my advisor, Dr. Yun-Shik Lee, for his help and patience with me during this entire endeavor. To Dr. Oksana Ostroverkhova, for always being available for questions and being extremely informative in both classwork and research. Finally, to my predecessors Andy Jameson, Joe Tomaino, and Michael Paul, for sharing their knowledge with me and allowing me to work alongside them in a fun research environment.

Personal

I am eternally indebted to the efforts of my parents, Philip and Rosemary Maizy, for without them this dream would have never even began and it is for them that I have chased it. To Anthony Jefferies, for being my motivation and rock whenever I doubted myself. To Megan McChesney, whose enduring friendship and support allowed me to get as far as I have. To all my friends and their neverending moral support, especially when all I had to offer in return were complaints. Finally, to the Brew Station and all it entails, for allowing me many a fun time and an outlet for said complaints.

TABLE OF CONTENTS

	<u>Page</u>
1. INTRODUCTION TO TERAHERTZ SPECTROSCOPY	1
1.1. Terahertz Radiation	1
1.2. THz Generation Methods	2
1.2.1 Titanium Sapphire - Ti:Sapph	3
1.2.2 Optical Rectification	3
1.2.3 Zinc Telluride - ZnTe	4
1.3. Detection Methods	4
1.3.1 Electro-optic Sampling	5
1.3.2 Bolometer	6
1.4. Carbon Nanotubes	7
1.5. Deposition Methods	8
1.5.1 LPCVD	9
1.5.2 PECVD	9
2. ELLIPSOMETRY	10
2.1. Index Ellipsoid	11
2.2. Fresnel Equations	13
3. TIME-DOMAIN SPECTROSCOPY	17
4. SAMPLE ANISOTROPY	21
4.1. Power Transmission	21
4.1.1 S-polarization Transmission	22
4.1.2 P-polarization Transmission	24
4.1.3 Discussion	25
5. CONCLUSION	26

TABLE OF CONTENTS (Continued)

	<u>Page</u>
1. APPENDIX A	27
BIBLIOGRAPHY	30

LIST OF FIGURES

<u>Figure</u>	<u>Page</u>
1.1 The electromagnetic spectrum, including the THz gap that is now being explored.	2
1.2 Diagram of how Kerr lens modelocking is achieved.	3
1.3 The generated pulse is the envelope of the incident optical pulse due to optical rectification.	4
1.4 Generalized setup of THz detection by electro-optic sampling.....	5
1.5 Polarization changes in electro-optic sampling.	6
1.6 Schematic of the inner workings of the bolometer.	7
2.1 Measurement principle of ellipsometry.....	10
2.2 Characterization of physical properties by spectroscopic ellipsometry.	11
2.3 Index ellipsoid for a uniaxial ($n_x = n_y < n_z$) material.	12
2.4 A generalized view of the sample with the nanotubes grown vertically on the substrate.	13
2.5 Transmission through the air-CNT-Si system.	13
3.1 SEM images of each of the LPCVD samples (L5b, L5a, and G5 respectively)....	18
3.2 Air reference THz spectra.	19
3.3 TDS frequency results for each sample using s-polarized THz radiation.	19
3.4 TDS frequency results for each sample using p-polarized THz radiation.	20
4.1 Diagram of the rotational stage setup for the power transmission measurements..	21
4.2 Bolometer power measurements of the silicon and blank substrates for both polarizations.	22
4.3 Theoretical versus experimental data regarding the transmission for the blank sample [s-polarization].....	23
4.4 Bolometer power measurements and theoretical data for s-polarization across all samples.	23
4.5 Theoretical versus experimental data regarding the transmission for the blank sample [p-polarization].	24
4.6 Bolometer power measurements and theoretical data for p-polarization across all samples.	25

LIST OF FIGURES (Continued)

<u>Figure</u>	<u>Page</u>
A.1 TDS of vertical CNT for both the PECVD and LPCVD samples.	27
A.2 Fourier transform of the TDS data of vertical CNT on both samples.	28
A.3 SEM images of each of the PECVD samples [(a) L5b, (b) L5a, (c) G5].	29

TERAHERTZ TRANSMISSION & SPECTROSCOPY OF VERTICALLY GROWN MULTI-WALLED CARBON NANOTUBE FORESTS

1. INTRODUCTION TO TERAHERTZ SPECTROSCOPY

1.1. Terahertz Radiation

Terahertz (THz) radiation refers to electromagnetic waves propagating at frequencies in the terahertz range. This range is defined as those frequencies which lie between the microwave and infrared regions of the spectrum. Refer to figure 1.1 for a visual guide to the electromagnetic spectrum. The following table shows typical values for quantities used in spectroscopy, centered around the frequency of 1 THz [1]:

- Frequency: $\nu = 1 \text{ THz} = 1000 \text{ GHz}$
- Angular Frequency: $\omega = 2\pi\nu = 6.28 \text{ THz}$
- Period: $\tau = 1/\nu = 1 \text{ ps}$
- Wavelength: $\lambda = c/\nu = 0.3 \text{ mm} = 300 \mu\text{m}$
- Wavenumber: $\bar{k} = k/2\pi = 1/\lambda = 33.3 \text{ cm}^{-1}$
- Photon Energy: $h\nu = \hbar\omega = 4.14 \text{ meV}$
- Temperature: $T = h\nu/k_B = 48 \text{ K}$

Up until recently, there existed what is known as the THz gap, which refers to the range of frequencies in the THz band that were relatively unexplored in science. The reason for this

was because of the difficulties involved in creating compact and efficient sources and detectors for THz radiation. In the last few decades, however, many advancements have been made to make exploring this THz gap possible.

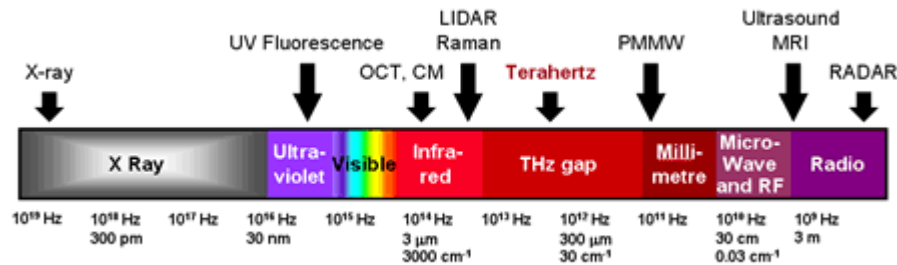


FIGURE 1.1: The electromagnetic spectrum, including the THz gap that is now being explored.

THz radiation now has many research areas and applications thanks to advancements made in the field. These include things such as medical imaging, since THz radiation has relatively low photon energy so as to not damage tissue and DNA; security purposes, such as detecting hazardous or illegal materials by their unique spectral response in the THz range; also for scientific use and imaging, such as time-domain spectroscopy (THz-TDS) and submillimeter astronomy.

This thesis will focus briefly on common generation and detection methods for THz radiation, then switch to the research I have done using these methods. I will present both theoretical and experimental data on the material properties of vertically grown carbon nanotube forests and their anisotropic response in the THz range.

1.2. THz Generation Methods

There are several common methods to generate terahertz radiation, all involving ultrashort pulses from titanium sapphire lasers. By name, these are using surface emitters, photoconductive emitters, and invoking a process called optical rectification. The latter is the one being focused on in this description.

1.2.1 Titanium Sapphire - Ti:Sapph

Titanium sapphire lasers are tunable lasers that emit red to near-infrared light. This corresponds to a general wavelength range of 650 to 1100nm. Ti:sapph refers to the lasing medium, which is a crystal of sapphire (Al_2O_3) doped with titanium ions. These lasers are usually pumped by another laser with a wavelength of 514-532nm, either an argon-ion laser (514.5nm) or frequency-doubled Nd:YAG laser (527-532nm). Pumping is the act of energy transfer from an external source to the gain medium of a laser.

Ti:sapph lasers are commonly used because of their great tunability and ease in generating ultrashort pulses of light. These ultrashort pulses can be generated with passive modelocking, usually in the form of Kerr lens modelocking. This process relies on the optical Kerr effect, which is a change in the refractive index of a material in response to an applied electric field. The laser pulse resonates back and forth inside a laser cavity where the non-linear medium lies, generating a train of output pulses. An adjustable slit on the cavity forces Kerr lens modelocking by suppressing the continuous-wave modes of low power while short pulses of high power are allowed to pass through the hard aperture.

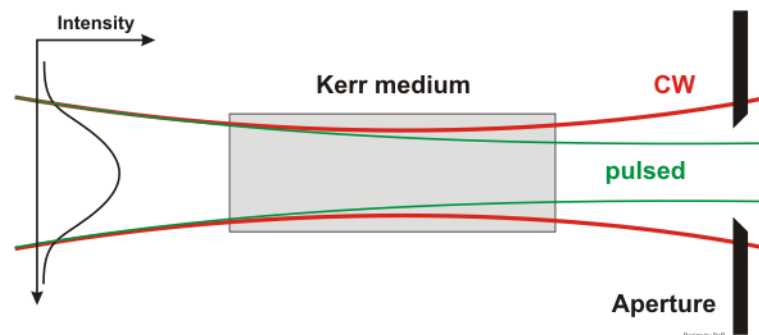


FIGURE 1.2: Diagram of how Kerr lens modelocking is achieved [2].

1.2.2 Optical Rectification

Optical rectification is a second order non-linear optical process in which a laser pulse creates a time-dependent polarization that radiates an electric field. The word “rectification” is

used because the rapid oscillations of the electric field of the laser pulse are “rectified” and only the envelope of the oscillations remains.

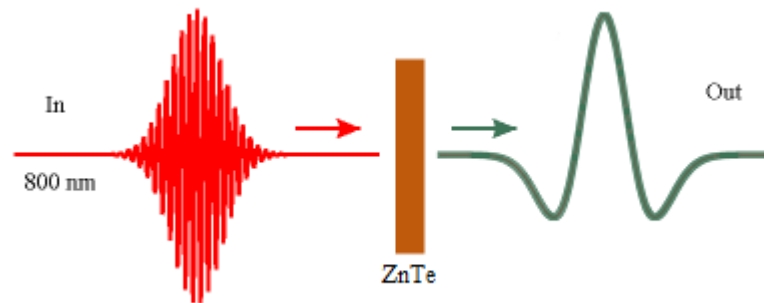


FIGURE 1.3: The generated pulse is the envelope of the incident optical pulse due to optical rectification.

This is a second-order non-linear process and therefore can only take place in materials that lack inversion symmetry (such as ZnTe). The bandwidth of the pulses are limited by the laser pulse duration, terahertz absorption in the crystal, the thickness of the crystal, and a mismatch between the propagation speed of the laser pulse and its speed within the crystal.

1.2.3 Zinc Telluride - ZnTe

ZnTe is a popular material for generating radiation in the 0.5-3 THz range and it was used for the duration of these experiments. THz pulses are generated when the crystal is irradiated with 800nm (near-infrared) laser pulses with a duration of around 100 femtoseconds through the aforementioned process of optical rectification.

1.3. Detection Methods

There are several ways to detect THz radiation, often grouped into two types: coherent and incoherent. The former allows detection of the waves with the amplitude and phase information

being provided, while the latter only gives intensity information. I will discuss two particular ways that were involved in the experiments performed.

1.3.1 Electro-optic Sampling

Electro-optic (EO) sampling is a coherent detection method that relies on a phenomenon known as the Pockels effect. This is a non-linear effect in which the refractive index of a material is modified in proportion to an applied electric field. In the case of THz radiation, the incident pulse induces a birefringence in an electro-optic medium that is proportional to the electric field of the pulse [3]. It can be used to measure THz waveforms in the time domain.

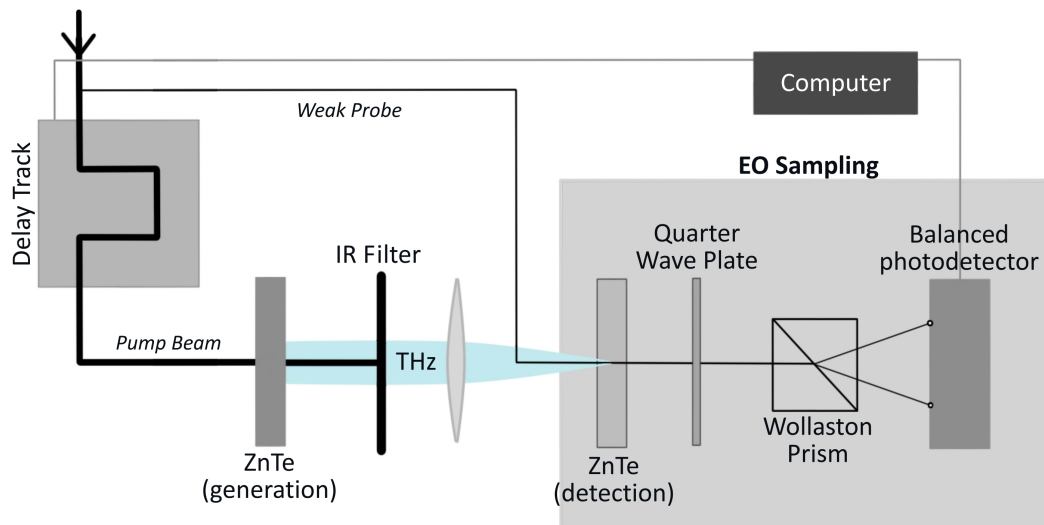


FIGURE 1.4: Generalized setup of THz detection by electro-optic sampling.

THz waveform measurements use a pump-probe setup. This means the initial laser pulse is separated by a beam splitter into a strong pump pulse as well as a weak probe pulse. The pump beam is used to generate the THz radiation (see sections 1.2.2/1.2.3) and the probe pulse has some time delay introduced into it. They are then recombined at a detection crystal, which is where the Pockels effect takes place. This effect rotates the polarization of the probe beam, which is then sent through a quarter wave plate ($\frac{\lambda}{4}$). This in turn makes the polarization almost circular, but with

just enough ellipticity that one component is noticeably larger. A Wollaston prism is then able to separate the beam into its components, which are then incident onto a balanced photodetector [see figure 1.4]. This detector is then able to measure the difference in intensity of the two polarizations, and by varying the time delay between the pump and probe pulses, time-resolved THz waveforms are obtained. Figure 1.5 is a diagram of the polarization changes that occur.

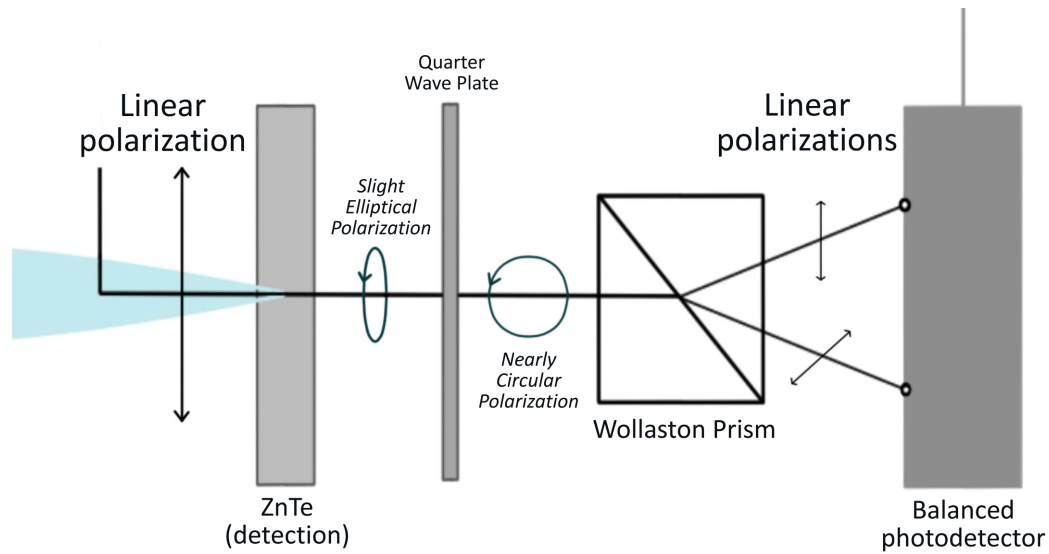


FIGURE 1.5: The polarization changes that occur which allow the mapping of the THz pulse.

1.3.2 Bolometer

The bolometer is an incoherent detection device used for measuring the energy of electromagnetic radiation. This works by having an absorptive element, such as a semiconductor or superconductor (silicon in our case), connected to a heat sink through a thermal link. When the incident radiation hits the element, the energy of the radiation raises its temperature. The difference in temperature from this and the heatsink can be measured by an attached thermometer, and from this the amount of power transmitted can be deduced. Most modern bolometers operate at cryogenic temperatures, which are attained by the use of coolants such as liquid helium. The one used in our experiments was cooled as such and operated at a temperature of 4K.

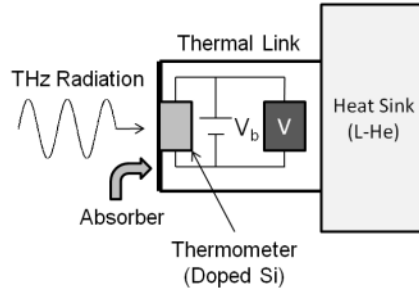


FIGURE 1.6: Schematic of the inner workings of the bolometer.

A downside to this technique is that, since it is based upon thermal changes, its detection speed is generally slow. It can detect very small THz intensities due to its sensitivity, but the response time is generally between 0.1-1 ms. Therefore, if information such as frequency spectra, time evolution or phase information is required, electro-optic sampling is the preferred method.

1.4. Carbon Nanotubes

Carbon nanotubes (CNTs) have become an extremely popular item in science within the last 20 years [4–12]. This is due to their remarkable physical and mechanical properties, such as having a thermal conductivity higher than diamond to having a strength, stiffness and resilience that exceeds many current materials. A CNT can behave differently depending on its structure, switching from a semiconductor to a semi-metal or metal. However, in the THz frequency range, the optical responses from the material are largely from the metallic CNTs [13, 14].

There are various growth methods for CNTs. Previously, nanotubes were grown along the substrate surface. Through recent scientific advancements, however, carbon nanotubes are now able to be grown vertically on, or orthogonal to, a substrate. This creates nanotube forests, which exhibit unique properties. These forests are ideal black materials in the visible and IR bands, absorbing light perfectly at all angles [15, 16]. In our experiments, we investigated optical properties of these structures in the THz region. We performed power transmission measurements

and time-domain spectroscopy on the samples to gain insight into these properties.

Multi-walled CNTs (MWCNT) are made in a similar fashion as single-walled CNTs (SWCNTs), which are an atomic monolayer of graphite (also referred to as graphene) curled over to form a cylindrical structure, however there are multiple layers of graphene initially present, so upon curling the layers, the structure consists of concentric cylinders. The interlayer distance in MWCNTs is close to the distance between graphene layers in graphite, which is approximately 3.4\AA [17]. These structures are easier to make than SWCNTs, however their behavior is less understood because of the complexity arising from interactions between the layers. The anisotropic nature of multi-walled CNTs is shown to be markedly different from that of single-walled CNTs because of electron transport between the shells [18].

1.5. Deposition Methods

Of the samples that were experimented upon, there were two different growth methods for the nanotube forests: low-pressure chemical vapor deposition [LPCVD] and plasma-enhanced chemical vapor deposition [PECVD]. Chemical vapor deposition is a chemical process used to produce high-purity, high-performance solid materials (most often thin films). During CVD, the substrate is prepared with a layer of metal catalyst particles (commonly nickel, cobalt or iron) so that the diameters of the nanotubes grown are related to the size of the particles. To initiate the growth of the nanotubes, two gases are bled into a reactor: a process gas (typically ammonia, nitrogen or hydrogen), and a carbon-containing gas (such as acetylene, ethylene, ethanol or methane). The nanotubes will then grow at the sites of the metal catalyst: the carbon-containing gas is broken apart at the surface of the catalyst particle, and the remaining carbon is then transported to the edges of the particle where it forms the nanotubes.

1.5.1 LPCVD

LPCVD is performed at subatmospheric pressures, which tend to reduce the unwanted gas-phase reactions in the deposition chamber and improve the uniformity of the film on the substrate. Most modern CVD processes are either done in this method, or in the lower pressure UHVCVD, which is ultra-high vacuum CVD. The substrates used to create the samples in this method were composed of a combination of aluminum oxide and iron ($\text{Al}_2\text{O}_3/\text{Fe}$).

1.5.2 PECVD

PECVD is a process used to deposit thin films on a substrate from a gas (vapor) state to a solid state. A plasma of the reacting gases is created by an AC RF frequency or DC discharge between two electrodes, and then chemical reactions occur to deposit the new solid onto the substrate. The nanotubes will grow in the direction of the electric field, which, by adjusting the geometry of the reactor, can be directed to make the nanotubes grow perpendicular to the substrate (also known as nanotube forests). The substrates used to create the samples in this method were composed of a combination of silicon dioxide and nickel (SiO_2/Ni).

2. ELLIPSOMETRY

Ellipsometry is an optical technique for the investigation of the dielectric properties (complex refractive index or dielectric function) of thin films. The key feature of ellipsometry is that it measures the change in polarized light upon light reflection on or light transmission by a sample. Typically, it measures two values: (ψ, Δ) . These are known as the amplitude ratio (ψ) and the phase difference (Δ) between light waves. The waves are classified as s- and p-polarized, which means that the incoming light is oriented perpendicular or parallel to the plane of incidence, respectively.

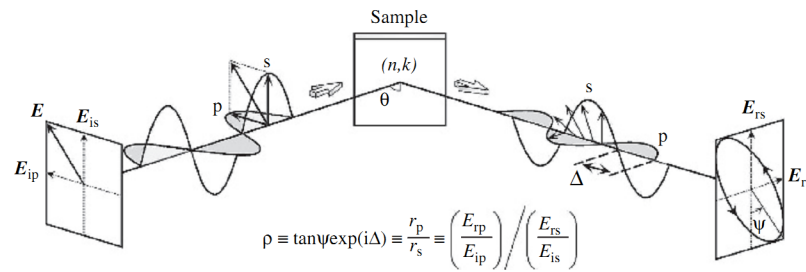


FIGURE 2.1: Measurement principle of ellipsometry. [19]

Unlike reflectance or transmittance measurements, ellipsometry allows the direct measurement of the refractive index n and extinction coefficient k , which are also referred to as optical constants [19]. From these, the complex refractive index can be found, which is defined as $N \equiv n - ik$. In the THz region, it is possible to gain information regarding free-carrier properties, such as conductivity. When a sample structure is simple, the amplitude ratio ψ is characterized by **the refractive index n** , whereas the phase difference Δ represents the light absorption described by **the extinction coefficient k** .

Generally speaking, there are several restrictions on this method. For one, the roughness of the samples being examined must be minimal. Secondly, the measurement must be performed at an oblique incidence. Ellipsometry measurements determine a polarization state from its light

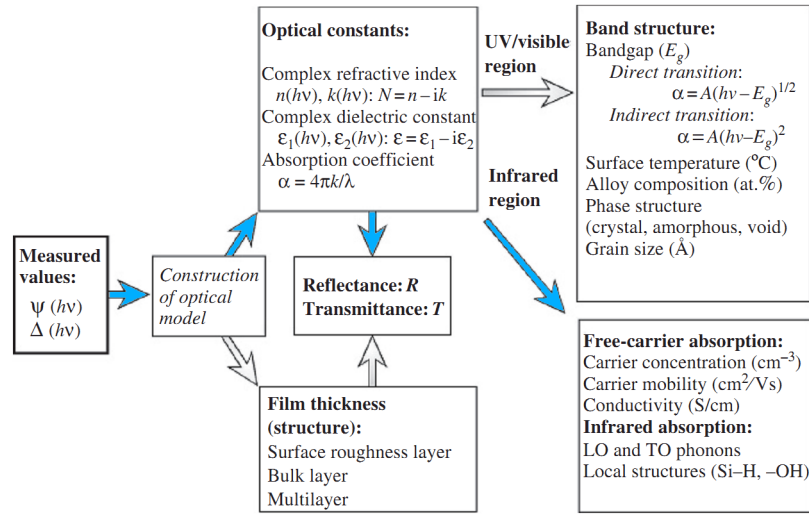


FIGURE 2.2: Characterization of physical properties by spectroscopic ellipsometry. [19] The highlighted arrows refer to properties investigated during the experiments run for this thesis.

intensity, so if the reflected light is too weak or scattered, the measurement cannot be made.

2.1. Index Ellipsoid

Anisotropic materials can broadly be classified into two types: biaxial and uniaxial. This distinction is with respect to the complex refractive indices of the material. Biaxial is defined as all complex refractive indices being different [$N_x \neq N_y \neq N_z$], whereas uniaxial is defined as only a single index being different [$N_x = N_y \neq N_z$]. By definition, the optical response of anisotropic materials changes with the orientation of the samples. Light reflection and transmission are described by \mathbf{E} [electric field] and \mathbf{S}_p [pointing vector], while the propagation of light is expressed by \mathbf{D} [electric displacement] and \mathbf{K} [propagation vector, $|\mathbf{K}| = 2\pi n/\lambda$]. Due to this, the optical constants of the materials must be described by a three-dimensional index ellipsoid. The energy density of the propagating light can be defined as:

$$U_E = \frac{1}{2} \mathbf{E} \cdot \mathbf{D} \quad (2.1)$$

From basic electromagnetic theory, we know that $\mathbf{D} = \epsilon \cdot \mathbf{E}$. Inserting this into the previous equation shows the following:

$$U_E = \frac{1}{2\epsilon_0} \left(\frac{D_x^2}{\epsilon_x} + \frac{D_y^2}{\epsilon_y} + \frac{D_z^2}{\epsilon_z} \right) \quad (2.2)$$

This result comes from the dot product of $\mathbf{D} \cdot \mathbf{D}$. By defining the following variables:

$$x = D_x / \sqrt{2\epsilon_0 U_E}, y = D_y / \sqrt{2\epsilon_0 U_E}, z = D_z / \sqrt{2\epsilon_0 U_E} \quad (2.3)$$

we can come to the recognizable result for the equation of a three-dimensional ellipse:

$$\frac{x^2}{\epsilon_x} + \frac{y^2}{\epsilon_y} + \frac{z^2}{\epsilon_z} = 1 \quad (2.4)$$

Since $\epsilon = n^2(k=0)$, the semiaxes of this ellipsoid correspond to the refractive indices along the x , y , and z axes [19].

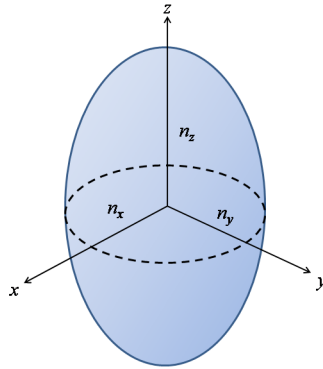


FIGURE 2.3: Index ellipsoid for a uniaxial ($n_x = n_y < n_z$) material.

Figure 2.3 represents the index ellipsoid of a positive uniaxial material. Since $n_x = n_y < n_z$, the semiaxis for z is longer, hence forming the ellipse. The cross-section of the x - y plane is a circle, so when \mathbf{K} is parallel to the z -axis, the index of refraction becomes a constant. Note that one of the semiaxes of the cross-section is always $n_0 = n_x = n_y$ within a uniaxial material.

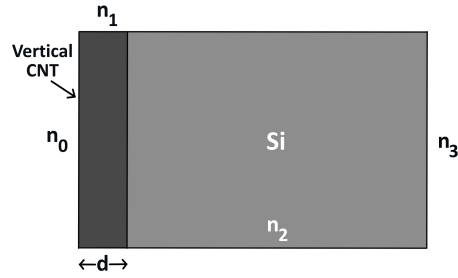


FIGURE 2.4: A generalized view of the sample with the nanotubes grown vertically on the substrate.

2.2. Fresnel Equations

In the case of an anisotropic film (in this case, the V-MWCNTs) on an isotropic substrate (Si), the effect of optical interference within the film must be taken into account. For the power measurements, the bolometer does not temporally resolve the initial pulse of the laser from the reflections within the sample, so all transmitted power is measured at once. Since there is no frequency data obtained, the calculations must sum over all reflections. Figure 2.5 is a visual representation of this idea. The multiply reflected waves can be related to each other by use of Snell's law ($N_0 \sin \theta_0 = N_2 \sin \theta_2$), where N_0 and N_2 are the refractive indices of air and the silicon substrate, respectively.

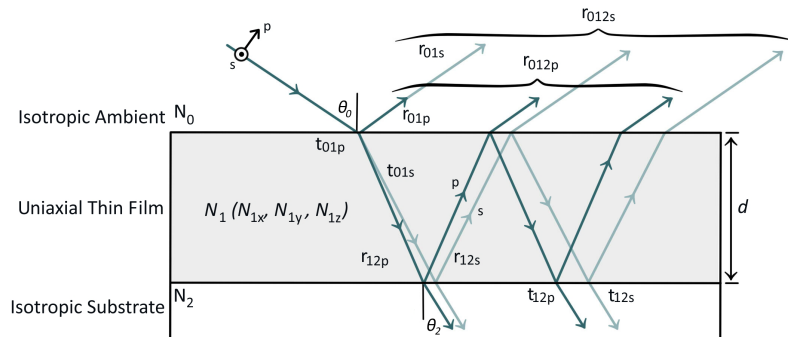


FIGURE 2.5: Transmission through the air-CNT-Si system.

Assume that the sample is divided into the following number scheme: 0 - air, 1 - CNT, 2 - Si, and 3 - air [see figure 2.4]. Figure 2.5 only shows the transmission through to the back of the Si substrate, but not through to air where it would be seen by our detector. Therefore, we need to include an extra term to account for that final part of transmission. The angle-dependent Fresnel equations for isotropic media are:

$$r_{jk,p} = \frac{n_k \cos \theta_j - n_j \cos \theta_k}{n_k \cos \theta_j + n_j \cos \theta_k} \quad r_{jk,s} = \frac{n_j \cos \theta_j - n_k \cos \theta_k}{n_j \cos \theta_j + n_k \cos \theta_k} \quad (2.5a)$$

$$t_{jk,p} = \frac{2n_j \cos \theta_j}{n_k \cos \theta_j + n_j \cos \theta_k} \quad t_{jk,s} = \frac{2n_j \cos \theta_j}{n_j \cos \theta_j + n_k \cos \theta_k} \quad (2.5b)$$

The variables θ_j and θ_k refer to the incident angles into each part of the system. For an anisotropic thin film [CNTs], the equations become modified. If the incoming pulses are p-polarized, the reflection and transmission coefficients for the air-CNT-Si system can be defined as follows:

$$r_{01p} = \frac{N_{1x}N_{1z} \cos \theta_0 - N_0(N_{1z}^2 - N_0^2 \sin^2 \theta_0)^{1/2}}{N_{1x}N_{1z} \cos \theta_0 + N_0(N_{1z}^2 - N_0^2 \sin^2 \theta_0)^{1/2}} \quad (2.6)$$

$$t_{01p} = \frac{2N_0 \cos \theta_0 [N_0^2 \sin^2 \theta_0 (N_x^2 - N_z^2) + N_z^4]^{1/2}}{N_z [N_z N_x \cos \theta_0 + N_0(N_z^2 - N_0^2 \sin^2 \theta_0)^{1/2}]}$$

$$r_{12p} = \frac{N_2(N_{1z}^2 - N_2^2 \sin^2 \theta_2)^{1/2} - N_{1x}N_{1z} \cos \theta_2}{N_2(N_{1z}^2 - N_2^2 \sin^2 \theta_2)^{1/2} + N_{1x}N_{1z} \cos \theta_2} \quad (2.8)$$

$$t_{12p} = \frac{2N_z^2 N_x (N_z^2 - N_0^2 \sin^2 \theta_0)^{1/2}}{[N_0^2 \sin^2 \theta_0 (N_x^2 - N_z^2) + N_z^4]^{1/2} [N_z N_x \cos \theta_2 + N_2(N_z^2 - N_0^2 \sin^2 \theta_0)^{1/2}]} \quad (2.9)$$

For an s-polarized pulse:

$$r_{01s} = \frac{N_0 \cos \theta_0 - (N_{1y}^2 - N_0^2 \sin^2 \theta_0)^{1/2}}{N_0 \cos \theta_0 + (N_{1y}^2 - N_0^2 \sin^2 \theta_0)^{1/2}} \quad (2.10)$$

$$t_{01s} = \frac{2N_0 \cos \theta_0}{N_0 \cos \theta_0 + (N_{1y}^2 - N_0^2 \sin^2 \theta_0)^{1/2}} \quad (2.11)$$

$$r_{12s} = \frac{(N_{1y}^2 - N_2^2 \sin^2 \theta_2)^{1/2} - N_2 \cos \theta_2}{(N_{1y}^2 - N_2^2 \sin^2 \theta_2)^{1/2} + N_2 \cos \theta_2} \quad (2.12)$$

$$t_{12s} = \frac{2(N_{1y}^2 - N_2^2 \sin^2 \theta_2)^{1/2}}{(N_{1y}^2 - N_2^2 \sin^2 \theta_2)^{1/2} + N_2 \cos \theta_2} \quad (2.13)$$

These take into account the fact that the CNTs are a uniaxial thin film. Generally speaking, the formulae for p-polarizations are more complicated due to the fact that \mathbf{D} and \mathbf{E} are not parallel to each other, as they are with s-polarization. For the power transmission measurements, we were concerned with the total transmission of the pulses through the entire sample. Taking into account each transmission and reflection yields the following sum:

$$t_{012} = t_{01}t_{12}e^{-i\beta} + t_{01}t_{12}r_{10}r_{12}e^{-i3\beta} + t_{01}t_{12}r_{10}^2r_{12}^2e^{-i5\beta} + \dots \quad (2.14)$$

$$r_{012} = r_{01} + t_{01}t_{10}r_{12}e^{-i2\beta} + t_{01}t_{10}r_{10}r_{12}^2e^{-i4\beta} + t_{01}t_{10}r_{10}^2r_{12}^3e^{-i6\beta} + \dots \quad (2.15)$$

Both of these equations have the form of a geometric series. This can be used to simplify both of them by observing the following identity:

$$\sum_{n=0}^{\infty} ar^n = a + ar + ar^2 + ar^3 + \dots = \frac{a}{1-r} \quad (2.16)$$

Applying this series summation to the previous transmission/reflection equations then yields the following formulae:

$$t_p = t_{012p} = \frac{t_{01p}t_{12p} \exp(-i\beta_p)}{1 + r_{01p}r_{12p} \exp(-i2\beta_p)} \quad (2.17)$$

$$t_s = t_{012s} = \frac{t_{01s}t_{12s} \exp(-i\beta_s)}{1 + r_{01s}r_{12s} \exp(-i2\beta_s)} \quad (2.18)$$

The variables β_p and β_s are phase variations for each type of wave, and can be defined as such:

$$\beta_p = \frac{2\pi d}{\lambda} \left(\frac{N_{1x}}{N_{1z}} \right) (N_{1z}^2 - N_0^2 \sin^2 \theta_0)^{1/2} \quad (2.19)$$

$$\beta_s = \frac{2\pi d}{\lambda} (N_{1y}^2 - N_0^2 \sin^2 \theta_0)^{1/2} \quad (2.20)$$

where d is the thickness of the film and λ is the wavelength of the incident radiation [around $300\mu\text{m}$ in our case].

For the total transmission exiting the sample with the nanotubes, we must include the transmission and reflection of the Si(2)-air(3) boundary. We can define the following sets of equations:

$$t_{\text{CNT},1\text{st}} = t \cdot t_{23} e^{i\varphi_s} \quad (2.21a)$$

$$t_{\text{CNT},2\text{nd}} = t \cdot r_{23} \cdot r \cdot t_{23} e^{3i\varphi_s} \quad (2.21b)$$

$$t_{\text{CNT},3\text{rd}} = t \cdot r_{23}^2 \cdot r^2 \cdot t_{23} e^{5i\varphi_s} \quad (2.21c)$$

These are the first three transmission equations through the entire system. Note that t in this case refers to $t_{p/s}$. Any term that is labeled (23) can use the standard angle-dependent Fresnel equations (2.5), as the substrate is isotropic and does not require separate indices of refraction. To get total transmitted power, we sum these up as we did for equations (2.17) and (2.18).

$$T_{\text{CNT}} = t^2 t_{23}^2 + t^2 t_{23}^2 (r \cdot r_{23})^2 + t^2 t_{23}^2 (r \cdot r_{23})^4 + \dots \quad (2.22)$$

$$\Rightarrow T_{\text{CNT}} = \frac{t^2 t_{23}^2}{1 - r^2 \cdot r_{23}^2} \quad (2.23)$$

It is also necessary to determine the transmission through just the substrate without the nanotubes ($d \rightarrow 0$). For the blank substrate:

$$t_{\text{Si},1\text{st}} = t_{02} \cdot t_{23} e^{i\varphi_s} \quad (2.24a)$$

$$t_{\text{Si},2\text{nd}} = t_{02} \cdot r_{23} \cdot r_{20} \cdot t_{23} e^{3i\varphi_s} \quad (2.24b)$$

$$t_{\text{Si},3\text{rd}} = t_{02} \cdot r_{23}^2 \cdot r_{20}^2 \cdot t_{23} e^{5i\varphi_s} \quad (2.24c)$$

These terms can also be defined using equation (2.5), as everything in the system is isotropic. Summing these up as before:

$$T_{\text{Si}} = t_{02}^2 t_{23}^2 + t_{02}^2 t_{23}^2 (r_{02} \cdot r_{23})^2 + t_{02}^2 t_{23}^2 (r_{02} \cdot r_{23})^4 + \dots \quad (2.25)$$

$$\Rightarrow T_{\text{Si}} = \frac{t_{02}^2 t_{23}^2}{1 - r_{20}^2 \cdot r_{23}^2} \quad (2.26)$$

The relative power transmission is then found by evaluating $T_{\text{CNT}}/T_{\text{Si}}$.

3. TIME-DOMAIN SPECTROSCOPY

THz time-domain spectroscopy [THz-TDS], this technique involves measuring changes in both the amplitude and phase of THz pulses induced by a sample, which provides enough information to simultaneously determine the absorption and dispersion of the sample. One can switch back and forth from the time domain to the frequency domain by taking the Fourier transform of the pulses. This technique is used to characterize the electromagnetic response of the material, such as permittivity and permeability. Another reason it is useful is that it provides a non-destructive probe for local carrier dynamics of metallic thin films [20, 21].

The method behind THz-TDS is similar to the pump-probe technique. As shown in figure 1.4, a beam splitter is used to separate the incoming optical beam into two parts. One part goes through the translational stage to provide a time delay relative to the other beam. The remaining pump beam goes through the terahertz emitter and generates terahertz radiation, which then gets focused onto the detector after passing through the sample. The time-delayed probe pulse measures the terahertz-induced transients in the detector.

As with a typical pump-probe setup, scans were set up for various amounts of time intervals. The transmitted THz waveforms can later be Fourier transformed to provide transmission data in the frequency domain.

The analysis done in this thesis was all based upon the spectrally integrated material responses. The frequency dependent responses obtained from the TDs data were analyzed by a more sophisticated theoretical model elsewhere [18].

There are 5 samples that have been experimented on, and they are named as such: silicon, blank, L5a/b, and G5a. Silicon is a standard silicon substrate, and blank is the silicon substrate with the growth catalyst for the CNTs applied to it.

Table 3.1 shows the different samples and their thicknesses. Refer to figure 3.1 for SEM images of the LPCVD samples. Upon visual inspection, the samples show near perfect black-

Sample	Thickness
G5	132 μm
L5a	62.5 μm
L5b	21.5 μm

TABLE 3.1: A breakdown of the different sample names and their thicknesses.

ness. This perfect blackness, however, disappears in the THz region because the spacing between adjacent CNTs (around 100 nm) is negligible compared with the wavelengths of THz radiation.

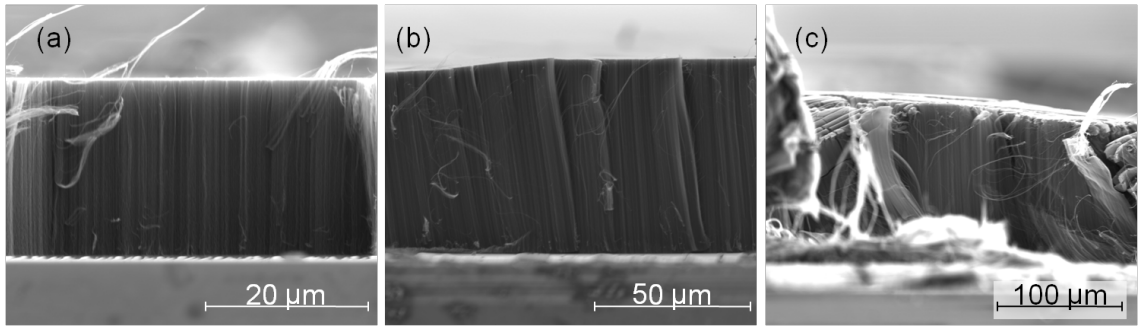


FIGURE 3.1: SEM images of each of the LPCVD samples (L5b, L5a, and G5 respectively).

Initially, air references were made to see the spectrum of the THz source. Note that the spectra in fig. 3.2 show peaks around 1THz. The next step was to run the same experiments on each of the samples. Figure 3.3 shows the results for the s-polarization frequency runs on each sample. As with fig. 3.3, fig. 3.4 shows the results for the p-polarization frequency runs on each sample. Most of the results gathered from the TDS data shows a peak response near 1THz as well. This was therefore the frequency used to do the theoretical modeling described in section 4.

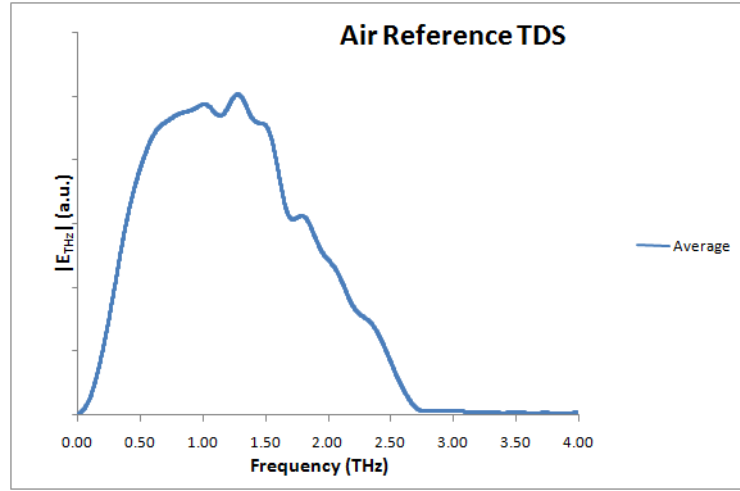


FIGURE 3.2: Air reference THz spectra.

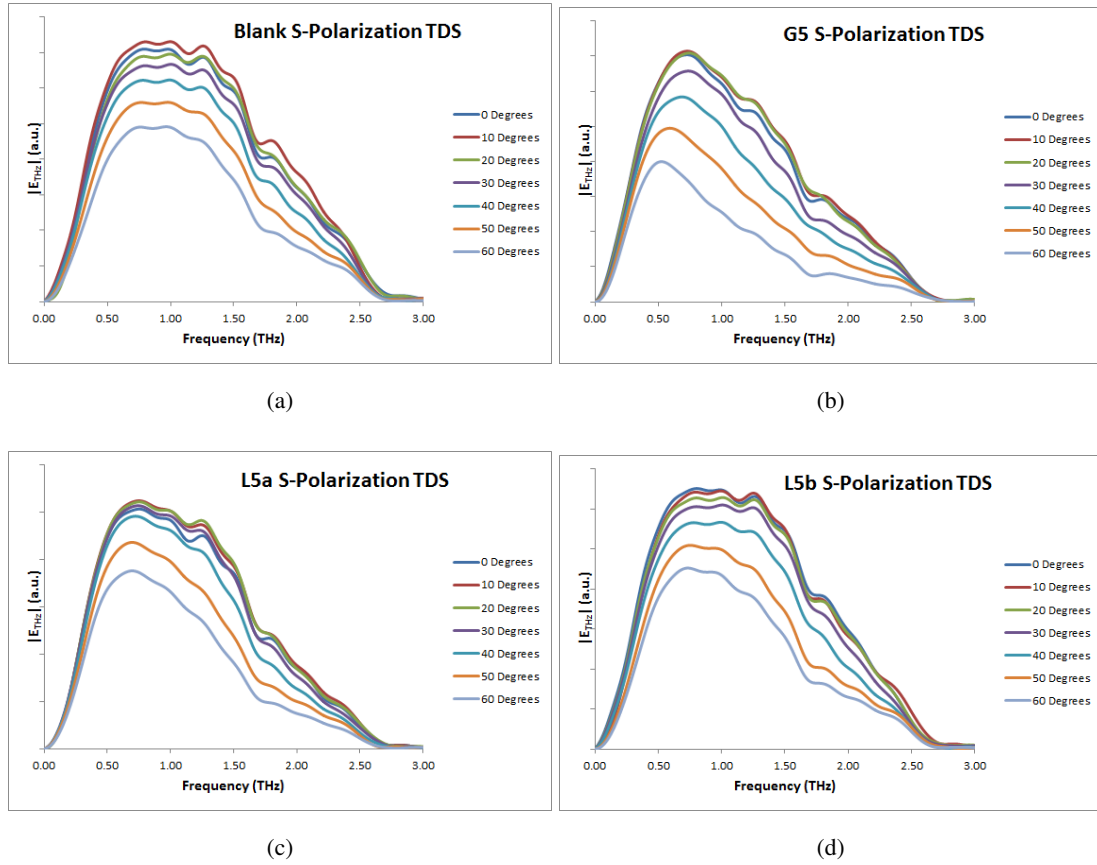


FIGURE 3.3: TDS frequency results for each sample using s-polarized THz radiation.

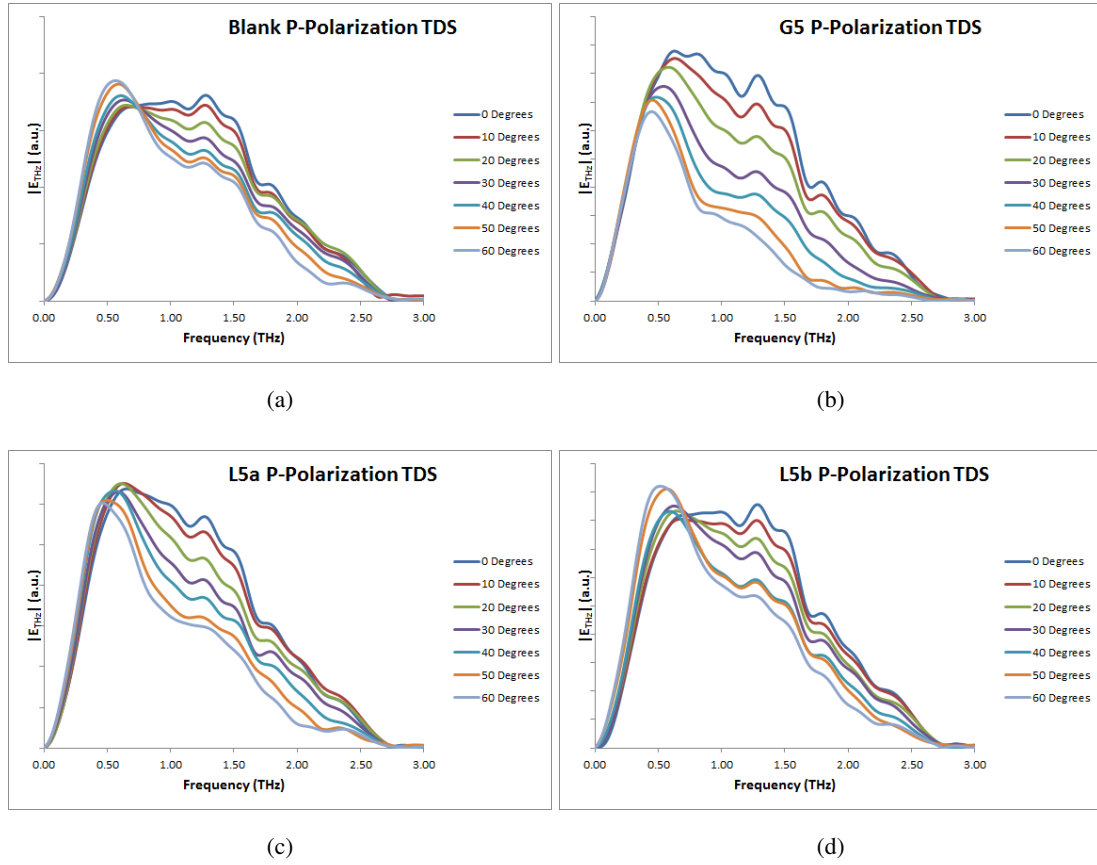


FIGURE 3.4: TDS frequency results for each sample using p-polarized THz radiation.

4. SAMPLE ANISOTROPY

As previously stated, when experimenting on the CNT samples, the incoming THz radiation was set up to be linearly polarized either perpendicular to the CNTs [s-polarization] or set up with a component parallel to the CNTs [p-polarization]. To do this, a rotational stage was inserted into the experimental setup to allow angle-dependent measurements for both polarizations.

In order to test the angle-dependent power transmission, each sample was set in the rotating stage and the bolometer was used to record the data. See figure 4.1 for a diagram of the setup.

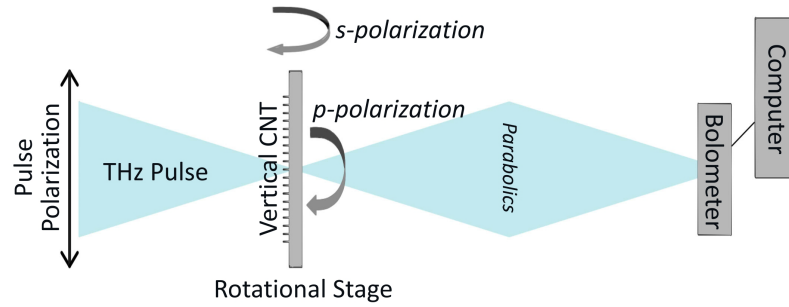


FIGURE 4.1: Diagram of the rotational stage setup for the power transmission measurements.

4.1. Power Transmission

Initially, tests were ran to observe the differences between the silicon and blank samples. As seen in figure 4.2, the data retrieved for these samples in both polarizations showed very similar trends, which indicates that the growth catalyst applied to the substrates has no significant effect on the THz transmission, therefore only the blank sample was used for further analysis. All data was taken for $\pm 60^\circ$, with 0° being the normal incidence and the step size as 1° . This is because finding the 0° mark so that it is normal to the incident beam can be tricky, so rotating in both directions allows us to find the best spot to mark as 0° . For a silicon sample, as the angle increases

[with p-polarization], the field amplitude [transmission] should increase and shift slightly in time, which figure 4.2 verifies. The s-polarization follows the opposite trend due to the E-field only being in the xy -plane [along the substrate].

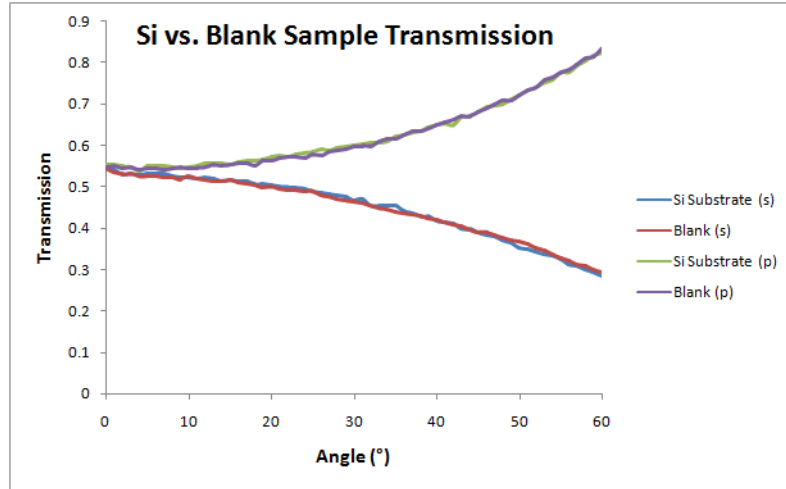


FIGURE 4.2: Bolometer power measurements of the silicon and blank substrates for both polarizations. Note the letter in the parentheses after each legend item refers to the polarization.

4.1.1 S-polarization Transmission

As stated, s-polarization implies that the CNTs were always perpendicular to the THz field. The silicon and blank samples showed a decrease in transmission as the angle increased.

To start, theoretical modeling was applied to the blank sample in order to test the viability of the theory. This sample was chosen due to its less complicated nature [ie. having no CNTs grown on it], as silicon is an isotropic medium and should follow the basic theory. After applying the theoretical modeling described in section 2.2., I was able to show that the experimental data retrieved for the blank sample matched closely with our theory.

This was relatively easy due to the fact that it did not involve any variables regarding the CNTs. Note that figure 4.3 is a relative measurement with respect to air. The main unknown in this system was the index of refraction of the CNTs. In order to test the theory, I chose a value for the index of refraction to work with (initially $n_{xy} = 1.14 - 0.28i$) at 1 THz [18]. Figure 4.4

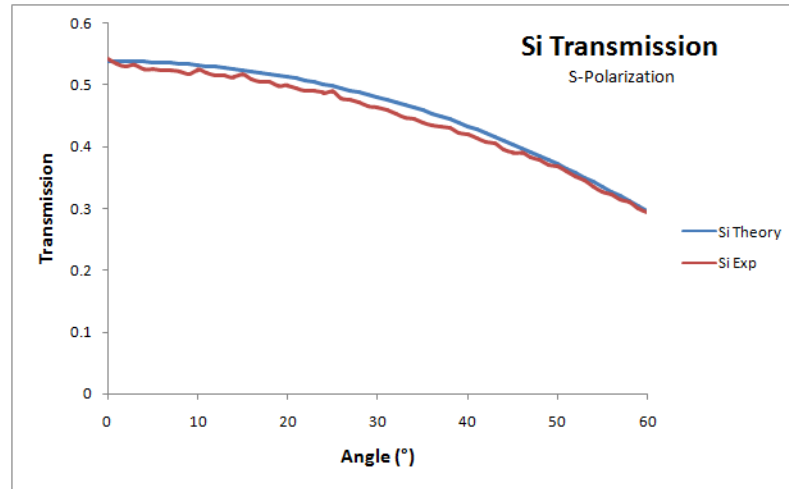


FIGURE 4.3: Theoretical versus experimental data regarding the transmission for the blank sample [s-polarization].

shows the results of the theoretical modeling compared to the experimental data retrieved.

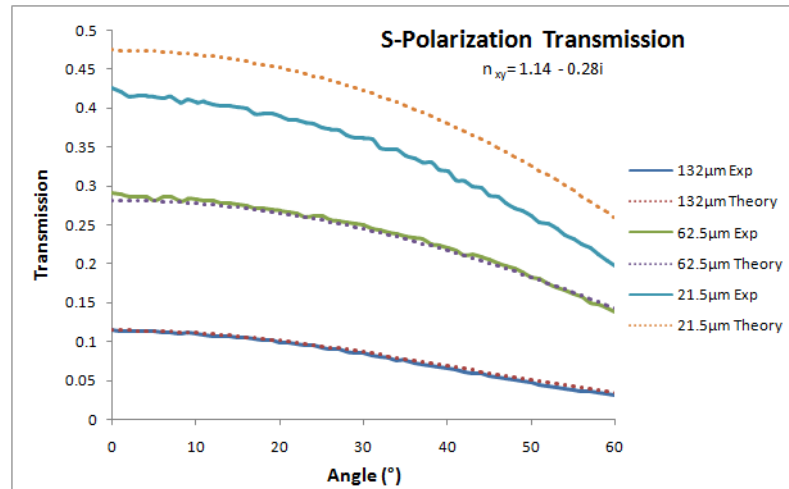


FIGURE 4.4: Bolometer power measurements and theoretical data for s-polarization across all samples.

Upon comparison, one can see that the theory and experiment match for two of the three samples. Although the third theoretical transmission [$21.5\mu\text{m}$] matches in shape, it is shifted about 5% in magnitude. The discrepancy mainly comes from the simplified theory being independent

of frequency.

4.1.2 P-polarization Transmission

For p-polarization, a THz field is composed of two components, one parallel and one perpendicular to the CNTs. The silicon and blank samples showed an increase in transmission as the angle increases, which is consistent with the optical properties of isotropic media. The CNT samples show a similar trend for small growth lengths, but it is in fact opposite as they get thicker. The transmission actually decreases with the thickest CNT sample at larger angles, much like the s-polarization transmission. This means that CNTs show anisotropy in the THz responses.

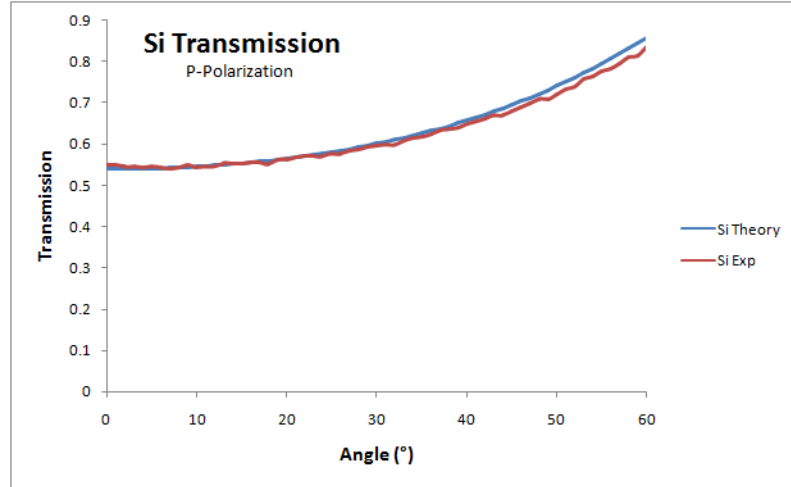


FIGURE 4.5: Theoretical versus experimental data regarding the transmission for the blank sample [p-polarization].

Figure 4.5 is the analysis for the blank sample. The theory matched experimental values, so I continued with further analysis for the CNT samples. Since the incoming radiation is p-polarized, \mathbf{D} and \mathbf{E} are not parallel to each other as they are with s-polarization. This also gives rise to separate indices of refraction, n_{xy} and n_z . Again, referring to [18], I set an initial value of $n_z = 1.26 - 0.7i$. Note that n_{xy} is the same as the s-polarization case, so the same value of $n_{xy} = 1.14 - 0.28i$ was used. Figure 4.6 shows the comparison of experimental and theoretical values of the transmission.

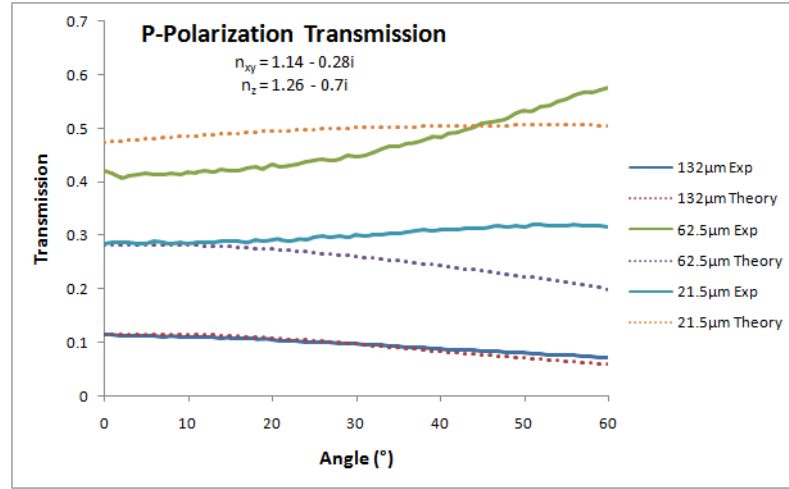


FIGURE 4.6: Bolometer power measurements and theoretical data for p-polarization across all samples.

As with the s-polarization analysis, the theory only partially matched the experimental data. The 132μm sample matched perfectly yet again, however the 62.5μm sample begins to deviate shortly after the angle begins to increase and the 21.5μm sample is yet again shifted by around 5% but not consistent with the data this time.

4.1.3 Discussion

A possible reason for disagreement in the results is that the assumptions used [the material has a frequency independent response] is too simplified, therefore yielding incorrect results. An approach using a more sophisticated frequency dependent model was performed in [18]. This involved modeling the vertical CNT film as a planar uniaxial dielectric material with a polarization that is governed by independent damped-driven oscillator dynamics. The parameters of this oscillator were extracted by using a Nelder-Mead nonlinear least squares algorithm. These numerical fitting methods allowed more accurate plots of the behavior of these CNTs, showing that they are in fact frequency dependent.

5. CONCLUSION

Although up until recently there existed what is known as the “terahertz gap”, or the range of frequencies in the THz band that were previously unexplored in science, this gap has been rapidly decreasing in size as more and more research is being done within it. This includes the research I performed on the anisotropic response of vertically grown carbon nanotubes.

The first result shown was that the nanotubes’ response to THz radiation was different depending on the polarization of incoming light. Experimentally, the power transmission through the nanotubes decreased with increasing angle for each sample when using s-polarized light. The considerably strong THz response along the xy -plane indicates that charge carrier transport occurs between neighboring shells in MWCNTs. For the p-polarized light, however, the transmission increased for the thinner two of the three samples with larger angles but decreased with the thickest of the samples.

Vertical SWCNTs are completely anisotropic, with responses only along the growth axis. The complex indices of refraction for the MWCNT samples were found to be $n_{xy} = 1.14 - 0.28i$ and $n_z = 1.26 - 0.7i$ for the s- and p-polarization, respectively. This relatively weak anisotropy indicates that THz fields can readily induce electron transport between neighboring shells. When applying theoretical modeling to these samples, three of the six trendlines matched the transmission patterns shown in the experiment. This leads me to believe that the assumptions being made in the theory are too simplified to get an exact match on the experimental data. If the analysis done was frequency-dependent, ie. the material’s response is different at different frequencies, then the results might have been more accurate. However, this still gives a good head start into the understanding of the behavior of vertically grown multi-walled carbon nanotube forests and their response to terahertz radiation.

1. APPENDIX A

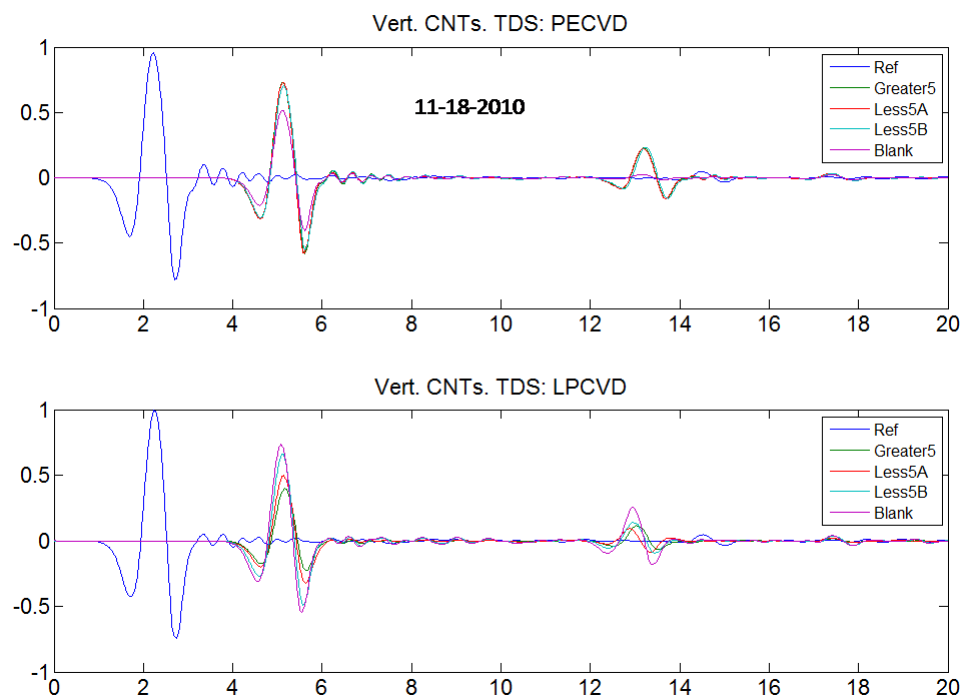


FIGURE A.1: TDS of vertical CNT for both the PECVD and LPCVD samples. Note the multiple waveforms mapped out over time, which indicate the multiple reflections through the sample.

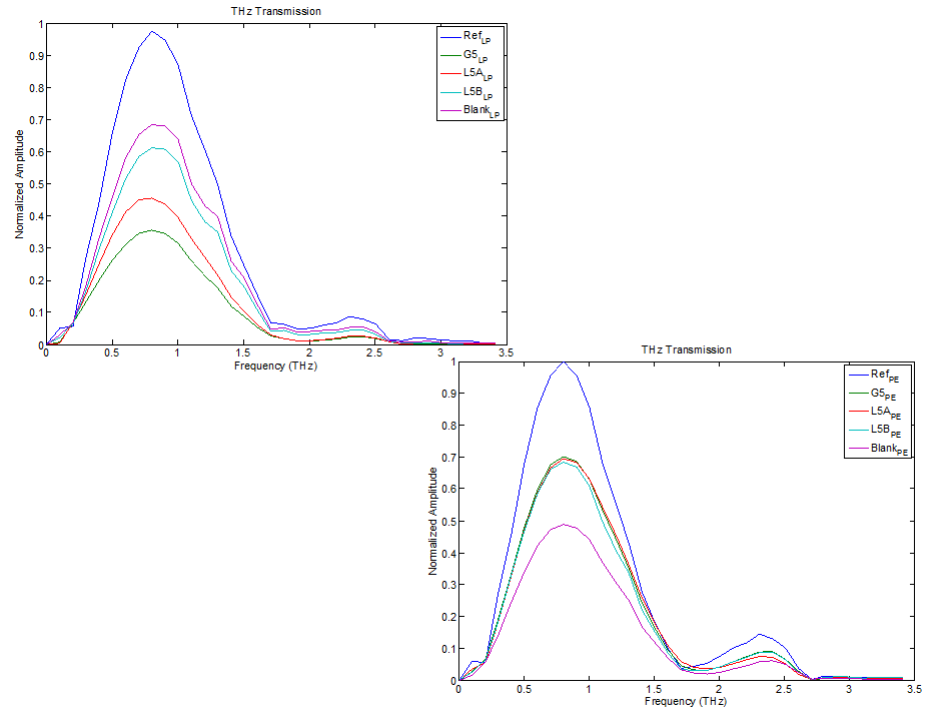


FIGURE A.2: Fourier transform of the TDS data of vertical CNT on both samples.

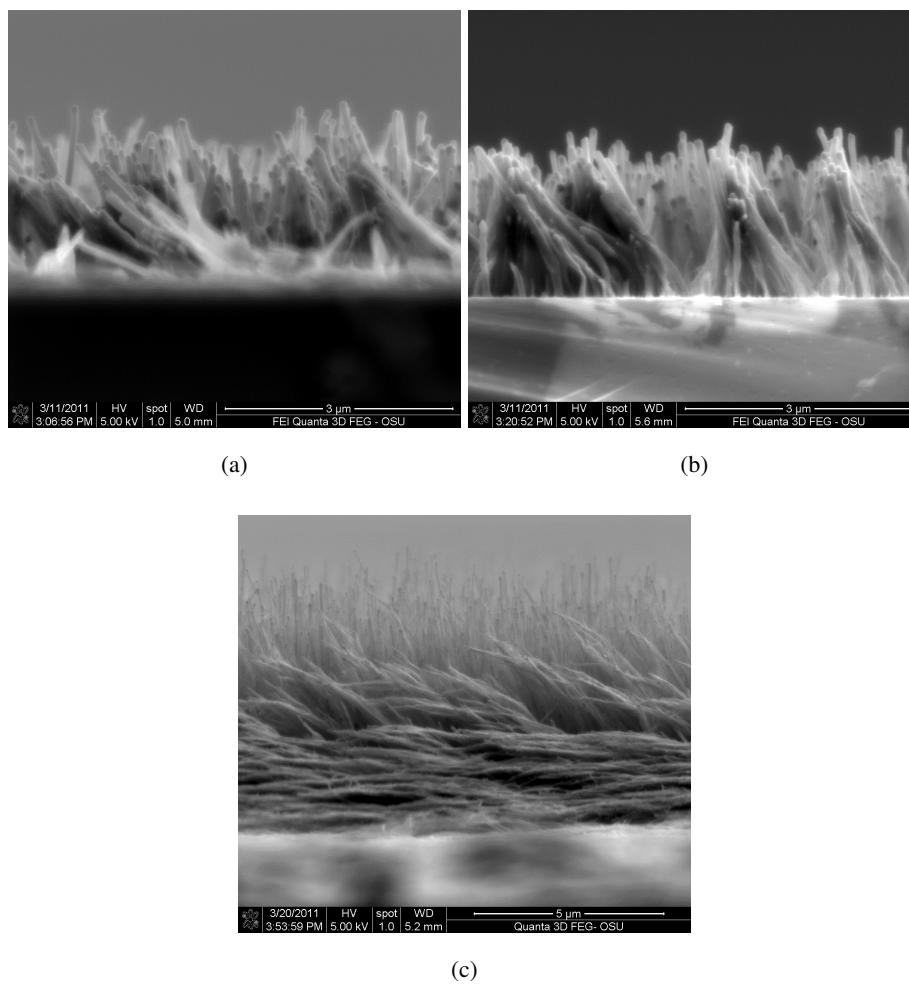


FIGURE A.3: SEM images of each of the PECVD samples [(a) L5b, (b) L5a, (c) G5].

BIBLIOGRAPHY

1. Y.S. Lee. *Principles of Terahertz Science and Technology*. Lecture Notes in Physics. Springer, 2008.
2. Wikipedia. Kerr-lens modelocking — wikipedia, the free encyclopedia, 2011.
3. M. Cooper, M.B. Johnston, G. Jotzu, and P. Parkinson. Electro-optic sampling. <http://www-thz.physics.ox.ac.uk/spectrometer/EOS.html>, 2009.
4. M.S. Dresselhaus, G. Dresselhaus, and P C. Eklund. *Science of Fullerenes and Carbon Nanotubes*. Academic Press, 1996.
5. Pulickel Ajayan and Otto Zhou. Applications of carbon nanotubes. In Mildred Dresselhaus, Gene Dresselhaus, and Phaeton Avouris, editors, *Carbon Nanotubes*, volume 80 of *Topics in Applied Physics*, pages 391–425. Springer Berlin / Heidelberg, 2001.
6. Ray H. Baughman, Anvar A. Zakhidov, and Walt A. de Heer. Carbon nanotubes—the route toward applications. *Science*, 297(5582):787–792, 2002.
7. Thomas W. Ebbesen. *Carbon nanotubes: preparation and properties*. CRC Press, 1997.
8. Boris I. Yakobson and Phaeton Avouris. Mechanical properties of carbon nanotubes. In Mildred S. Dresselhaus, Gene Dresselhaus, and Phaeton Avouris, editors, *Carbon Nanotubes*, volume 80 of *Topics in Applied Physics*, pages 287–327. Springer Berlin Heidelberg, 2001.
9. Erik T Thostenson, Zhifeng Ren, and Tsu-Wei Chou. Advances in the science and technology of carbon nanotubes and their composites: a review. *Composites Science and Technology*, 61(13):1899 – 1912, 2001.
10. P.J.F. Harris. *Carbon Nanotubes and Related Structures: New Materials for the Twenty-first Century*. Cambridge University Press, 2001.
11. K. Tanaka, T. Yamabe, and K. Fukui. *The Science And Technology Of Carbon Nanotubes*. Referex Engineering. Elsevier, 1999.
12. D.M. Guldi and N. Martín. *Carbon Nanotubes and Related Structures*. Wiley online library. Wiley, 2010.
13. Inhee Maeng, Chul Kang, Seung Jae Oh, Joo-Hiuk Son, Kay Hyeok An, and Young Hee Lee. Terahertz electrical and optical characteristics of double-walled carbon nanotubes and their comparison with single-walled carbon nanotubes. *Applied Physics Letters*, 90(5):051914, 2007.

14. M. A. Seo, J. H. Yim, Y. H. Ahn, F. Rotermund, D. S. Kim, S. Lee, and H. Lim. Terahertz electromagnetic interference shielding using single-walled carbon nanotube flexible films. *Applied Physics Letters*, 93(23):231905, 2008.
15. Zu-Po Yang, Lijie Ci, James A. Bur, Shawn-Yu Lin, and Pulickel M. Ajayan. Experimental observation of an extremely dark material made by a low-density nanotube array. *Nano Letters*, 8(2):446–451, 2008. PMID: 18181658.
16. Kohei Mizuno, Juntaro Ishii, Hideo Kishida, Yuhei Hayamizu, Satoshi Yasuda, Don N. Futaba, Motoo Yumura, and Kenji Hata. A black body absorber from vertically aligned single-walled carbon nanotubes. *Proceedings of the National Academy of Sciences*, 106(15):6044–6047, 2009.
17. Wikipedia. Carbon nanotube — wikipedia, the free encyclopedia, 2012.
18. M. J. Paul, N. A. Kuhta, J. L. Tomaino, A. D. Jameson, L. P. Maizy, T. Sharf, N. L. Rupesinghe, K. B. K. Teo, S. Inampudi, V. A. Podolskiy, E. D. Minot, and Yun-Shik Lee. Terahertz transmission ellipsometry of vertically aligned multi-walled carbon nanotubes. *Applied Physics Letters*, 101(11):111107, 2012.
19. Hiroyuki Fujiwara. *Spectroscopic Ellipsometry: Principles and Applications*. John Wiley & Sons, Chichester, England; Hoboken, NJ, 2007.
20. J. L. Tomaino, A. D. Jameson, J. W. Kevek, M. J. Paul, A. M. van der Zande, R. A. Barton, P. L. McEuen, E. D. Minot, and Yun-Shik Lee. Terahertz imaging and spectroscopy of large-area single-layer graphene. *Opt. Express*, 19(1):141–146, Jan 2011.
21. A. D. Jameson, J. W. Kevek, J. L. Tomaino, M. Hemphill-Johnston, M. J. Paul, M. Koretsky, E. D. Minot, and Yun-Shik Lee. Terahertz spectroscopy of ni-ti alloy thin films. *Applied Physics Letters*, 98(22):221111, 2011.

